Relation Between Void Ratio and Contact Fabric of Granular Soils

Yuxuan Wen[1] and Yida Zhang[2*]

Abstract

Void ratio is one of the key engineering properties of granular soils. It reflects how well the grains are packed and hints whether the soil is contractive or dilative upon shearing. On the other hand, fabric tensor has been at the centre of experimental and theoretical granular mechanics research over the past decade for its intimate relation with the material's anisotropy and critical-state behaviour. This paper tests the hypothesis that the void ratio and the fabric tensor of granular soils are tightly correlated to each other. Through discrete element method, a series of isotropic/anisotropic consolidation tests and monotonic triaxial compression and extension tests are conducted. The obtained void ratio data is found to collapse onto one unique surface, namely the fabric-void ratio surface (FVS), when plotted against the first two invariants of the contact-based fabric tensor. The robustness of this relation is confirmed by testing samples with different initial void ratios under various consolidation and monotonic triaxial stress paths. An additional undrained cyclic triaxial test followed by continuous shearing to critical state is performed to further examine the fabric-void ratio relation under complex loading paths. It is found that the previously identified FVS from monotonic tests still attracts the states of these specimens at critical state, although their fabric-void ratio paths deviate from the FVS during cyclic loading. The newly discovered FVS provides a refreshing perspective to interpret the structural evolution of granular materials during shearing and can serve as an important modelling component for fabric-based constitutive theories for sand.

Keywords Anisotropy · Discrete-element modelling · Fabric/structure of soils · Sands

[1] Graduate student, Dept. of Civil, Environ. and Architect. Eng., University of Colorado Boulder, Boulder, CO, USA

[2] Assistant Professor, Dept. of Civil, Environ. and Architect. Eng., University of Colorado Boulder, Boulder, CO, USA. Email: yida.zhang@colorado.edu

1 Introduction

Void ratio (or porosity) is the most widely used index by geotechnical engineers and soil mechanists to characterize the "state" of granular soils. The celebrated critical state soil mechanics framework uses void ratio to define critical state which further distinguishes dense and loose soils [1]. Void ratio (e) informs engineers how well the soil is packed [2] and its potential for liquefaction [3]. On the other hand, fabric structure characterized by the directional statistics of particles, voids, contact normal vectors is also tightly related to the macro-behaviour of granular soils including anisotropy [4, 5], non-coaxiality [6], critical state [7], and liquefaction [8]. However, despite both void ratio and fabric tensors are quantitative descriptors of soil internal structure, their interconnections are seldomly studied. A specific question is, can the fabric data be used to deduce the void ratio of granular materials? First of all, it is straightforward to see that void ratio is proportional to the hydrostatic component of void-based fabric tensors [9]. Such clear relation does not exist for particle- or contact-based fabric tensors. Many studies in the field of granular physics, powder technology and chemical engineering have been devoted to establishing a relation between e and the coordination number (Z), i.e., the first invariant of the non-normalized contact fabric tensor. For frictionless monodisperse granular assemblies, an e-Z relation can be pinned down by considering several idealized packings including cubic ($Z = 6$, $e = 0.9099$), orthorhombic ($Z = 8$, $e = 0.6540$), tetragonal–sphenoidal ($Z = 10$, $e = 0.4533$) and rhombohedral ($Z = 12$, $e = 0.3503$). A number of empirical e-Z equations have been also proposed for bi-disperse or polydisperse granular assemblies based on experiments and DEM simulations of gravitational stable or compressed specimens [10-15].

For general stress paths that involves shearing, the relation between Z and e is no longer unique. This can be demonstrated by considering an undrained test: if each e uniquely corresponds to one Z value, Z must be a constant during undrained shearing since e is kept constant. This is not supported by DEM experiments showing that undrained samples can liquefy where Z drops sharply [16-18]. It is thus inferred that e should at least also be a function of the fabric anisotropy (F), or equivalently the second invariant of contact fabric

tensor. Rothenburg and Kruyt [19] have similarly pointed out that the relationship between Z and e is affected by the anisotropy of contact orientations. Kruyt [20] showed that Z evolves with both volumetric and shear strains, implying that e may be a function of both Z and fabric anisotropy. Huang et al. [21] shows that the critical state e-Z relation is not unique and is dependent on the intermediate principal stress ratio b, and the variation of e is apparently related to F which is sensitive to b. They clarified that the increase of F with b is the cause of non-uniqueness of e-Z relation at critical state. In an attempt to integrate fabric tensor in the constitutive modeling of sand, Zhang et al. [22] suggested that a relation between e and soil fabric is imperative to unify the classical notion of critical state defined in the e-p-q space [1] (p is the mean effective stress, q is the deviatoric stress) and the recently discovered critical fabric surface (CFS) in the principal fabric space [23]. Hence, the fabric-void ratio relationship worth a systematic investigation for better understanding and modelling of the micro-macro behaviour of granular soils.

The objective of this paper is to study the linkage between void ratio and the non-normalized second-rank contact fabric tensor for granular soils. Towards this goal, a series of three-dimensional (3D) DEM simulations consists of consolidation, undrained, and drained monotonic triaxial tests are conducted (Section 2). The fabric tensor and the void ratio data are plotted in the e-Z-F space, through which a unique fabric-void ratio surface (FVS) is identified (Section 3). The FVS is then mathematically represented and further validated by additional DEM tests with various initial void ratios (Section 4). Finally, an undrained cyclic triaxial tests is performed to examine whether the proposed FVS can capture the fabric-void ratio data for samples experiencing stress reversals (Section 5). The significance of proposed FVS is discussed in Section 6. The main conclusions and possible future extensions of this work are discussed at the end (Section 7).

2 Methodology

2.1 DEM configuration

The open-source program YADE [24] is used in this study to carry out all DEM

simulations. Consolidation and triaxial tests are simulated employing periodical boundary conditions on a granular representative volume (REV) made of 10,000 sphere particles with a grain size distribution shown in Fig. 1. The choice of 10,000 particles is made to balance the computational efficiency and the representativeness of the granular specimen. Other DEM studies on granular REVs have used similar or fewer particles [25-27]. All particles are randomly generated without contacts in a 3 × 3 × 3 cm^3 box and then isotropically or anisotropically consolidated prior to shearing. Linear elastic contact law is adopted with the normal stiffness k_n and tangential stiffness k_s being $k_n/d = k_s/d = 100$ MPa, where d is the particle diameter. The normal and tangential interparticle forces between two particles with stiffness k_{n1}, k_{s1} and k_{n2}, k_{s2} are calculated by $F_n = K_n \delta_n = k_{n1} \cdot k_{n2} / (k_{n1} + k_{n2}) \delta_n$ and $F_s = K_s \delta_s = k_{s1} \cdot k_{s2} / (k_{s1} + k_{s2}) \delta_s$, where K_n, δ_n and K_s, δ_s are the stiffness and displacement of the contact in the normal and tangential direction. The interparticle friction is modelled by the Coulomb's law with the friction coefficient set to $\mu = 0.5$, a typical value for quartz sand [18, 28].

The simulation is conducted under quasi-static condition where the influence of particle mass (inertia) is negligible so that the density scaling technique can be adopted to reduce the computation cost [17, 29-31]. Specifically, the critical timestep of the system is related to the minimum particle size and elastic wave propagation speed by $\Delta t_{cr} = \min\left(R_i \sqrt{(\rho_g)_i / E_i}\right)$ [24], where subscript "i" represents the i^{th} particle, R the particle radius, ρ_g the particle density, and E the elastic modulus. By scaling the particle density from $\rho_g = 2.65 \times 10^3$ kg to 2.65×10^6 kg, Δt_{cr} is increased by a factor of $\sqrt{1000} = 31.62$, allowing the computation to accelerate by 31.62 times. For triaxial test simulations, the inertia number $I = \dot{\varepsilon} \bar{d} \sqrt{\rho_g / p}$ should be much less than 10^{-3} to ensure the quasi-static condition [32-35], where $\dot{\varepsilon}$ is the strain rate, $\bar{d}$ the average particle diameter, and p the mean effective stress. Through a parametric study, a strain rate of 0.05 s^{-1} is selected to ensure the maximum $I << 10^{-3}$ such that the quasi-static requirement is satisfied.

In DEM, a common method to control the initial void ratio of granular specimens is to

adjust the initial friction coefficient μ_0 when generate and initially compact the spheres before the official test program [31, 36, 37]. The use of a lower value of μ_0 eases the particle rearrangement during initial compaction and thus leads to a denser specimen, and vice versa. Note that the value of μ_0 must be less than μ, otherwise the sample will have sudden collapse at the moment when μ_0 is updated to μ. Since we are interested in the consolidation data in this study, it is necessary to update μ_0 to μ at the very early stage of compaction such that this operation does not interference with the consolidation and triaxial data which must reflect the behaviour of soils with μ=0.5. The procedure adopted in this study is the following: spheres are sparsely generated in a cubic regime according to the designated grain size distribution (Fig. 1) with μ_0 selected between 0 to 0.5; the periodic boundaries are moved inwards to isotropically consolidate the particles to p = 5kPa which is far less than the consolidation stresses p_c=50~2000 kPa studied in this work; μ_0 is then updated to μ = 0.5 and the remaining consolidation and triaxial shearing are conducted following the ordinary procedure.

2.2 Experiment design

Three series of DEM experiments are performed in this study. In the first series, μ_0 = 0.3 is used to create an initially medium-dense packing e_0 = 0.6437. Note that, throughout this paper, notation e_0 refers to the void ratio of the specimen at isotropic p = 50 kPa. The medium-dense samples are isotropically or anisotropically consolidated under various stress ratios η_0 = 0, 0.1, 0.2, 0.3, 0.4, 0.5, 0.6 and 0.7, as shown in Fig. 2. This is to probe the fabric-void ratio relation of granular packings during consolidation. For isotropically consolidated specimens, undrained (CIU) and drained (CID) triaxial tests are performed at various confining stresses p_c to allow the stress ratio η evolve from 0 to critical value. These are designed to cover a wide range of intermediate states in the fabric-void ratio space. Various intermediate principal strain and stress ratios with b_e = 0, 0.25, 0.5, 0.75, 1 and b = 0, 0.25, 0.5, 0.75, 1 are used in the CIU and CID tests to check the potential Lode-angle dependency of the fabric-void ratio relation. Here $b_e = (\varepsilon_2 - \varepsilon_3) / (\varepsilon_1 - \varepsilon_3)$ and $b = (\sigma_2 - \sigma_3)/(\sigma_1 - \sigma_3)$, where $(\varepsilon_1, \varepsilon_2, \varepsilon_3)$ and $(\sigma_1, \sigma_2, \sigma_3)$ are the major, intermediate, and minor principal strains and stresses, respectively. The testing details of the consolidation, CIU and CID tests are summarized in

Table 1.

To examine the effect of initial void ratio e_0 on the fabric-void ratio relation, another series of consolidation and triaxial tests on specimens prepared at different μ_0 values are performed. They are named C_e_0, CIU_e_0, and CID_e_0 tests, respectively (Table 2). These sample are prepared with μ_0 = 0.2 or 0.5 to obtain an initially dense (e_0=0.6174) or loose (e_0=0.6701) state, respectively.

Finally, an isotropically consolidated undrained cyclic triaxial (CIUC) test is performed to probe the fabric-void ratio relation under complex stress paths involving loading reversals. The CIUC test is conducted on the dense specimen (μ_0 = 0.2 and e_0 = 0.6174). Cyclic loading is applied after consolidation (p_c = 300kPa) in a stress-controlled manner with maximum deviatoric stress q_{max} = 150kPa. After cyclic loading for N = 20 cycles, the specimen is monotonically sheared until reaching critical state.

A total of 137 simulations are conducted in this study, including 8 consolidation tests, 40 CIU tests, 40 CID tests, 16 C_e_0 tests, 16 CIU_e$_0$ tests, 16 CID_e_0 tests and 1 CIUC tests.

2.3 Fabric tensor definition

We focus on contact-based characterization of soil fabric. For a given granular assembly, the directional distribution of contacts is given by:

$$\rho(\mathbf{n}) = \frac{2N_c}{N_p}\bar{\rho}(\mathbf{n}) \tag{1}$$

where $\mathbf{n}$ is the unit contact normal vector; $\bar{\rho}(\mathbf{n})$ is the distribution density; N_p the number of particles and N_c the number of contacts. The integration of $\rho(\mathbf{n})$ over all direction gives the coordination number, Z:

$$\int_{4\pi} \rho(\mathbf{n}) d\Omega = \frac{2N_c}{N_p} = Z \tag{2}$$

where $\Omega \in [0,4\pi]$ is the solid angle. Kanatani [38] defined three kinds of fabric tensors, with the first kind expressed as:

$$G_{ij} = \int_{4\pi} \rho(\mathbf{n}) n_i n_j d\Omega \tag{3}$$

where n_i with i = 1, 2, 3 is the component of the contact normal. It is straightforward to see

that the trace of G_{ij} is exactly the coordination number, i.e., $G_{kk} = Z$ and the discretized form of G_{ij} is:

$$G_{ij} = \frac{2}{N_p} \sum_{\alpha=1}^{N_c} n_i^{(\alpha)} n_j^{(\alpha)} \tag{4}$$

On the other hand, it is useful to approximate $\rho(\mathbf{n})$ by a 2nd order tensor:

$$\rho(\mathbf{n}) \approx \frac{1}{4\pi} E_{ij} n_i n_j \tag{5}$$

where the E_{ij} is the fabric tensor of the second kind [38]. It can be shown that the mean spherical part of E_{ij} is Z (i.e., $Z = E_{kk} / 3$) by integrating Eq. (5) over all directions. By multiplying Eq.(5) with $n_k n_l$ and integrating over $\Omega \in [0, 4\pi]$, the relation between E_{ij} and G_{ij} is obtained as:

$$E_{ij} = \frac{15}{2}\left(G_{ij} - \frac{1}{5} G_{kk} \delta_{ij} \right) \tag{6}$$

Finally, the fabric tensor of the third kind is simply the deviatoric part of E_{ij} which also has a linear relationship with the deviatoric part of G_{ij}:

$$F_{ij} = E_{ij} - \frac{1}{3} E_{kk} \delta_{ij} = \frac{15}{2}\left(G_{ij} - \frac{1}{3} G_{kk} \delta_{ij} \right) = \frac{15}{2} G'_{ij} \tag{7}$$

where the superscript $'$ means the deviatoric part. Substituting Eq.(7) into Eq.(5) gives:

$$\rho(\mathbf{n}) \approx \frac{1}{4\pi}\left(Z + F_{ij} n_i n_j \right) \tag{8}$$

which can be viewed as the spherical harmonic expansion of $\rho(\mathbf{n})$ truncated to the second order. The normalized fabric tensors of the first, second and third kind can be obtained with the same mathematical procedure with respect to $\bar{\rho}(\mathbf{n})$ instead of $\rho(\mathbf{n})$. Most of the previous DEM studies [36, 39, 40] have reported their fabric data in terms of normalized fabric tensors to focus on fabric anisotropy. However, the information of Z is lost in this representation, thus cannot reveal the full picture of fabric evolution for granular materials undergoing deformation. In analogous to using p and q where $p = \sigma_{kk} / 3$ and $q = \sqrt{(3/2)\sigma'_{ij}\sigma'_{ij}}$ to represent the stress state of soil specimens, here we use the first two invariants of the non-normalized contact fabric tensor E_{ij}, namely $Z = E_{kk} / 3$ and

$F = \sqrt{(3/2) F_{ij} F_{ij}}$, to monitor the fabric evolution and to correlate with void ratio in each test.

3 Fabric-void ratio surface

3.1 Consolidation tests

The consolidation lines in the *e-p* plane are plotted in Fig. 3a. The normal consolidation line (NCL) is best fitted by $e = \Gamma - \lambda \left(p / p_a \right)^{\xi}$ with p_a = 101.3 kPa (the atmosphere pressure), Γ = 0.6555, λ = 0.01832 and ξ = 0.7628. The consolidation lines of η_0 = 0.1 ~ 0.3 tests almost coincide with the NCL, and the lines of $\eta_0 \geq 0.4$ tests becomes lower when η_0 increases. The observation that the consolidation line locates lower for specimens consolidated at higher η_0 is consistent with previous findings [41-43]. The consolidation lines are plotted in the *e-Z* plane in Fig. 3b. Data from different η_0 tests deviates with each other at the beginning of consolidation but converges as *Z* increases. This proves that the *e-Z* relation is non-unique for frictional granular materials, as speculated in the *Introduction* session. Fig. 3c shows the fabric paths of consolidation tests in the *Z-F* plane. It is evident that higher η_0 lead to overall stronger fabric anisotropy during consolidation. Another observation is that *F* decreases with the increase of *Z* for $\eta_0 \geq 0.4$ tests, indicating reduced fabric anisotropy under high confining stresses. This is expected, as higher confining stress creates stronger and more connected force networks to support the same stress anisotropy with a weaker contact anisotropy. By combining Figs. 3a-c, the fabric-void ratio relation of consolidation tests in *e-Z-F* space is shown in Fig. 3d. More data is needed to probe the fabric-void ratio states in between the consolidation lines to tell whether a unique surface can be constructed.

3.2 Undrained (CIU) tests

The stress paths and stress-strain curves of CIU test under triaxial compression (b_e = 0) and extension (b_e = 1) conditions are presented in Fig. 4. It is observed that several tests under small p_c are liquefied while others reach critical state at around axial strain of 20-30%. The slopes of the critical state line (CSL) in *p-q* space for compression and extension tests are M_c = 0.77 and M_e = 0.61, respectively.

Figs. 5a and b shows the fabric paths of triaxial compression and extension tests,

211 respectively. The initial states of all samples are nearly isotropic with $F \approx 0$ and a Z value of
212 3.5~6. Upon shearing, fabric anisotropy F start to develop accompanied by the decrease of Z.
213 For liquefied specimens, their fabric paths quickly evolve towards the origin at the onset of
214 liquefaction as marked by the dash lines. As axial strain keeps increasing, the stresses of
215 liquefied specimens remain nearly zero (i.e., $p \approx q \approx 0$ kPa), while their fabric structures start
216 to rebuild as manifested by the development of a fabric path in the low Z regime, which
217 appears to be independent of the initial condition of the specimen. The fabrics of liquefied
218 samples finally reach steady state somewhere along this unique curve. Regarding the
219 minimum value of Z during liquefaction, Nguyen et al. [17] found that the Z of liquefied
220 samples directly evolve to a steady-state value 3.91 instead of dropping to 0 first, which is
221 different from the observations of Gu et al. [16], Wang and Wei [18], Wen and Zhang [23]
222 and the current paper. Wang et al. [44] showed that the value of Z drops to ~1 instead of 0
223 upon liquefaction. More studies on the fabric structure and coordination number of liquefied
224 frictional granular materials are needed to clarify these inconsistencies.

225 The fabric paths of non-liquefied specimens never drop below a threshold coordination
226 number (Z_{th}) and reached to some critical-state fabric (Z_c, F_c) when sheared to large strain
227 levels. Connecting the liquefied fabric path with the series of critical-state fabric data, it is
228 possible to construct a critical-state line in the Z-F plane that attracts the fabric states of both
229 liquefied and non-liquefied specimens when sheared to large strain levels (Figs. 5a and b).
230 This line can be mathematically represented by the Gunary equation
231 $F = Z / \left(a_1 + a_2 \sqrt{Z} + a_3 Z \right)$ where (a_1 = 1.05, a_2 = −1.17, a_3 = 0.755) for b_e = 0 tests and (a_1 =
232 0.82, a_2 = −0.58, a_3 = 0.49) for b_e = 1 tests. These envelopes are in fact projections of the
233 more general critical fabric surface (CFS) in the principal fabric (E_1-E_2-E_3) space, as recently
234 proposed by Wen and Zhang [23].

235 Fig. 5c plots all the fabric and void ratio data obtained from CIU tests in e-Z-F space.
236 Starting from the NCL shown in Fig. 3d, specimens with different p_c and b_e are sheared under
237 undrained condition which enforces a constant void ratio during shearing. The tests with p_c =
238 50 and 100 kPa are liquefied while other tests with higher p_c are not. It is observed that the

fabric-void ratio data seems to fall in two apparent regimes separated by Z_{th}. Data in $Z < Z_{th}$ belongs to liquefied specimens and $Z > Z_{th}$ for non-liquefied tests. It is also observed that for tests with $p_c \geq 300$ kPa, their fabric-void ratio relations are almost independent of the shear mode b_e, despite that the values of Z and F at critical state are b_e-dependent (see Fig. 5a and Fig. 5b). For liquefied specimens with $p_c = 50 \sim 100$ kPa, the fabric-void ratio data under different b_e condition also coincides with each other prior to liquefaction and roughly collapse into one line in the $Z < Z_{th}$ regime.

3.3 Drained (CID) tests

The CID tests results for $b = 0$ and $b = 1$ are shown Figs. 6a-b and Figs. 6c-d, respectively. It is observed from Fig. 6a and Fig. 6c that the critical state stress ratio is $M_c = 0.77$ for compression tests and $M_e = 0.61$ for extension tests, which is consistent with the CIU tests results shown in Figs. 4a and c. For the drained fabric paths in Figs. 6b and d, anisotropy F evolves from near zero to a peak and then drops to the critical state value. These critical fabric values again fall on the same CFS identified previously in the undrained tests (Figs. 5a and b). This again proves that CFS is independent of liquefaction or drainage conditions and can serve as an universal attractor for fabric state upon continuous shearing [23]. Fig. 6e plots the fabric data against the evolving void ratios obtained from CID tests. Similar to Fig. 5c, it is found that the fabric path in CID tests is independent of the shear mode b except near the critical-state values.

Fig. 7 combines the fabric-void ratio data obtained from consolidation, CIU, and CID tests presented in Figs. 3d, 5c, and 6e. An astonishing finding is that all the fabric-void ratio data for non-liquefied specimens visually collapse into one single surface which shall be referred to as the non-liquefied (NL) fabric-void ratio surface (FVS). The “state” of the sample (characterized by fabric and void ratio) simply travels along this surface via different paths when subjected to monotonic shearing. It is also noted that the post-liquefication data from CIU tests collapse into another surface (or line) in the low Z ($< Z_{th}$) regime and exhibits certain degree of scattering. Based on the observations in Figs. 5a and b, this surface can be regarded as the CFS for liquefied soils extended vertically along the void ratio axis, which

will be referred to as the liquefied (L) FVS. The L-FVS data only expands within a small range of e near the upper bound of NL-FVS in the e-Z-F space, since only very loose packing are liquefied in this series of CIU tests.

Note that the current fabric-void ratio relation is investigated in the e-Z-F space and the effect of the third invariant of E_{ij} or the fabric Lode angle θ_E is omitted. This appears to be a reasonable assumption since the shear mode b_e or b is observed to have little effect on the evolution of fabric-void ratio data in CIU and CID tests prior to reaching the critical state (see Figs. 5c and 6e), and there is not much data scattering around the FVS (see the next section for a quantitative evaluation) identified in the e-Z-F space including the near critical state regime (see Fig. 7). Therefore, θ_E will not be considered when we construct a model of the fabric-void ratio relation in the following.

4 Mathematical description and validation

We shall pursue a mathematical description of the FVS to evaluate the quality of the data correlation and to facilitate the integration of such surface in constitutive models for sands such as the critical fabric theory proposed by Zhang et al. [22]. In addition, the uniqueness of FVS will be validated using data from samples prepared to different initial densities (i.e., different e_0).

4.1 Mathematical description

For the non-liquefied portion of the FVS, a good starting point is the Z-n equation proposed by O'hern et al. [12] for isotropically or oedometrically compressed granular assemblies:

$$Z - Z_r = h\left(n - n_r\right)^{\varphi} \tag{9}$$

where n is the porosity; h and φ are material parameters; Z_r is the coordination number at a reference porosity n_r which is usually taken at the jamming point. Taking Eq. (9) as a reference for $e = f\left(Z, F\right)$ at $F = 0$, the mathematical expression of the NL-FVS is proposed as:

$$e = e_r + h_r \left(Z - Z_r \right)^{\zeta} + A_1 F + A_2 F^2 \tag{10}$$

where a second-order polynomial in terms of F is added to consider the effect of fabric anisotropy; e_r and Z_r are respectively the void ratio and coordination umber taken at the reference point; h_r, ζ, A_1 and A_2 are material parameters. Eq. (10) is best fitted to the NL-FVS data with parameters $e_r = 0.6641$, $Z_r = 3.258$, $h_r = -0.02898$, $\zeta = 2.0$, $A_1 = -0.02627$ and $A_2 = 0.004352$ with the accuracy quantified by $R^2 = 0.9852$ (Fig. 8).

For the liquefied portion (i.e., $Z <= Z_{th}$) of the FVS, we first examine the data on the Z-F plane, as shown in Fig. 9a, given all data in this portion comes from CIU tests conducted at similar void ratios. The fitted CFS curves for $b_e = 0$ and 1 in Figs. 5a and b are also plotted here in Fig. 9a. It is clear that the CFS is dependent on the shear mode, which is consistent with the observation of Wen and Zhang [23] who inspected the shape of CFS in the principal fabric space. For simplicity, here we adopt an averaged critical fabric curve with expression:

$$F = Z \Big/ \left(0.9937 - 1.044\sqrt{Z} + 0.7070 Z \right) \tag{11}$$

to represent this data cluster in the fabric-void ratio space (Fig. 9b). By doing so, we have hypothesized that averaged critical fabric curve or the L-FVS is independent of void ratio as long as the sample is fully liquefied. This assumption shall be further tested with more CIU tests conducted at a wider range of void ratios in the next section. For now, the L-FVS fitting gives a R^2 value of 0.9568, as shown in Fig. 9b.

The small scattering ($R^2 = 0.9852$ for NL-FVS and $R^2 = 0.9568$ for L-FVS) supports the existence of a unique FVS linking the void ratio and the first two invariants of contact fabric tensor for samples subjected to monotonic consolidation, undrained, and drained triaxial shearing. This surface exhibit weak dependency on the shear mode near critical state in both liquefied and non-liquefied regime. Comparing to the many e-Z models developed for gravity-filled granular packings in powder technology [15, 45-47], our proposed FVS depicts a more complete picture by incorporating the effect of fabric anisotropy on the density of granular assemblies. The new FVS concept is therefore applicable for conditions involving anisotropic consolidation and triaxial shearing which are relevant for soil mechanics applications, providing a new perspective to analyse the internal structure of granular soils.

4.2 Validation

The FVS in Figs. 8 and 9 is developed exclusively based on medium-dense samples prepared with $\mu_0 = 0.3$. To validate the uniqueness and the robustness of the FVS, additional tests including C_e$_0$, CIU_e$_0$ and CID_e$_0$ tests using relatively dense (prepared with $\mu_0 = 0.2$) and loose (prepared with $\mu_0 = 0.5$) samples are conducted, as summarized in Table 2.

Fig. 10 present the critical state data of CIU, CID, CIU_e$_0$ and CID_e$_0$ tests on the *e-p* and the *Z-p* planes. The conventional CSL in the *e-p* plane can be well represented by the power-law function of Li and Wang [48] as $e_c = 0.630 - 0.00365\left(p / p_a\right)^{1.202}$ where p_a = 101.3 kPa. The critical-state *Z-p* data also collapse into a single curve fitted by $Z_c = 2.779 + 0.679(p / p_a)^{0.441}$. These results confirm that the CSL in the *e-Z-p* space is independent of the sample's initial void ratio, shear mode, and drainage conditions, which is consistent with previous findings [16, 23, 49]. Fig. 11a compares the NCLs for the dense, medium dense, and loose samples in the *e-p* plane. Fig. 11b plots the corresponding NCLs in *e-Z* plane, or in other words the fabric-void ratio relation for isotropically consolidated samples ($F \approx 0$). It is observed that the *e-Z* curves are closely located in a narrow band (despite some slight variations in the dense regime) in contrast to the distinct curves in the *e-p* plane.

The previously constructed NL-FVS (Eq. (10)) and the fabric-void ratio data from the new C_e$_0$, CIU_e$_0$ and CID_e$_0$ tests are plotted together in Fig. 12a. It can be observed that the new data qualitatively falls on the same surface. For a specific fabric-void ratio data (Z_{data}, $F_{data,}$ e_{data}), its corresponding e on the FVS can be calculated by $e(Z_{data}, F_{data})$ using Eq. (10) and is denoted as e_{FVS}. The comparison of e_{data} and e_{FVS} is then shown in the Fig. 12b. The small scattering (R^2 =0.9700) quantitatively validates the uniqueness of the NL-FVS with respect to the initial densities of the specimens. It is noted that the e_{FVS} deviates slightly from the e_{data} in the very dense regime (around e_{data} = 0.45). This deviation could be due to several limitations of this study. First, the contact model is linear elastic which might be reasonable for low confining pressures but cannot represent real contacts (nonlinear, pressure-dependent) at high pressure levels. The error due to this idealization therefore shows up at dense packing

regime where high confining stress is applied. Second, the present study uses the first two invariants of E_{ij} (represented by Z and F) to correlate with void ratio. This approach neglects the information represented by θ_E, as well as the higher-order information contained in the full contact distribution density. Future enrichments of FVS considering the above may remove the deviations between e_{data} and e_{FVS}.

The data from liquefied specimens in CIU_e$_0$ test and the mathematical L-FVS (Fig. 9b) are plotted together in the Z-F plane (Fig. 13a) and in the fabric-void ratio space (Fig. 13b). The agreement between the data and the mathematical L-FVS (Eq. (11)) is quite well as evidenced by $R^2 = 0.9806$. The observation that the liquefied fabric data of all undrained tests with different e_0 can be represented by the same Z-F curve confirms our earlier hypothesis that the critical fabric curve is independent of void ratio in the liquefied regime, and thus validated the L-FVS proposed in Fig. 9b and Eq. (11). It is also observed in Fig. 13b that Z and F for denser soils evolves to larger values in the liquefied regime. This feature can be utilized to precisely locate the threshold Z (Z_{th}) that separates the liquefied and the non-liquefied states, i.e., by observing the maximum Z (Z_{max}) of the specimen with the minimum void ratio among all liquefied tests. The Z_{max} of all liquefied undrained tests presented in Figs. 9 and 13 is $Z_{max} = 2.73$ from the CIU_e$_0$ test with $e = 0.6171$ and $p_c = 50$ kPa. This means that the value of Z_{th} must be ≥ 2.73. On the other hand, it is interesting to note that the critical state Z_c at $p = 0$ calculated by the CSL equation in Fig. 10(b) is $Z_c(p=0) = 2.779$, which is quite close to Z_{th}. It is therefore reasonable to infer that the intersection $Z_c(p=0)$ in the power-law equation that fits the critical state Z-p data is not just a fitting parameter but has the physical meaning of the threshold Z that distinguishes the liquefied and non-liquefied soils.

5 Undrained cyclic (CIUC) test

We have demonstrated that the states (fabric, void ratio) of granular material travel along a single FVS during monotonic loading including consolidation, CIU, and CID tests. There are two aspects remain to be addressed: 1) it is unclear whether the same FVS works for stress paths involving loading reversals; 2) at the moment of static liquefaction, the fabric-

void ratio data jumps from the NL-FVS to the L-FVS and then stays on it, but it is not clear whether this sudden transition happens during cyclic liquefaction and whether liquefied states can evolve from the L-FVS back to the NL-FVS as shear strain accumulates. To answer these questions, a CIUC test is conducted on a dense sample with p_c = 300 kPa, q_{max} = 150 kPa and e = 0.5911. The specimen is subjected to a two-stage loading. The first stage is cyclic triaxial loading which stops when the number of cycles N reaches 20. After this, the specimen is monotonically sheared through triaxial compression to the critical state.

Figs. 14a-d show the stress-strain curve, the stress path, the fabric path, and the fabric-void ratio path from CIUC tests, respectively. It is observed from Figs. 14a and b that the specimen exhibits the typical cyclic liquefaction/mobility behaviour. In Fig. 14c, the fabric evolution path drifts to lower Z values during cyclic loading and jumps to the origin as soon as the sample liquefies. As shear continues, the fabric path evolves partially along the L-FVS and re-enters the non-liquefied regime ($Z > Z_{th}$=2.73 regime) where the sample regains some shear strength. The same phenomenon can be better visualized in the fabric-void ratio space in Fig. 14d. It is clear that the "butterfly" stress loop in Fig. 14b corresponds to a closed fabric path circulating between the L-FVS and the non-liquefied regime.

Figs. 14c and d confirm that the fabric-void ratio data during cyclic loading approximately stays on the L-FVS after liquefaction but does not stay on the NL-FVS before liquefaction. If the descriptor of soil's inner structure is sufficient, it should fully quantify the "memory" of the soil and exhibit a one-to-one relation with the macroscopic properties of the soil. We suspect that the non-uniqueness of FVS for monotonically and cyclically loaded specimens can be removed by considering higher-order fabric information which is not reflected in the 2nd-rank fabric tensor. Along this line, examining the full directional distribution density of contact normal may reveal some unique microstructural features of cyclically loaded granular materials.

The monotonic loading after the cyclic stage takes the specimen to its critical state and is marked by blue dot lines and red stars in Fig. 14. It is observed that the monotonic shearing eventually brings the cyclically loaded specimens back to the NL-FVS with the squared error

(SE) = 3.73×10^{-5}, confirming again the FVS identified in Fig. 8 could serve as a reference surface for granular materials under monotonic shearing, although it does not uniquely relate void ratio and fabric for cyclically loaded specimens.

6 Significance of FVS

With the FVS identified, a "so what" question naturally follows. We would like to make the case here that FVS can change how we conceive the constitutive theories and models of granular soils. Specifically, the fabric-void ratio relation proposed here connects two important state variables (void ratio and fabric), implying that the previously observed critical state line in the conventional *e-p-q* space [1] and fabric space [28] are not independent to each other. Indeed, the authors have recently proposed a constitutive framework, namely the critical fabric theory [22], where fabric is treated as the single internal state variable of granular soils. In this framework, the only criterion that judges whether a soil has reached critical state is to see if its fabric state converged to the critical fabric surface [23]. As the fabric evolves towards this CFS, the other state variables (*e-p-q*) approach their apparent critical state because of some geometrical or microstructural relations that link fabric with the void ratio and stress state of granular soils. To exercise this logic, let us combine the CFS (i.e., $F(Z)$ relation) under an arbitrary shear mode (e.g., compression or extension as shown in Figs. 5 or 6), a fabric-void ratio relation (FVS shown in Fig. 8), and a critical state *Z-p* relation (shown in Fig. 10(b)). A mathematical expression between *e* and *p* can be derived:

$$e = e_r + h_r\left[Z(p) - Z_r\right]^{\zeta} + A_1 F\left(Z(p)\right) + A_2 F^2\left(Z(p)\right) \tag{12}$$

where parameters e_r, Z_r, h_r, ζ, A_1 and A_2 are already calibrated in Fig. 8 and presented after Eq. (10). The obtained equation is plotted against the DEM critical-state data (Fig. 10(a)) in *e-p* plane in Fig. 15. It is apparent that the derived CSL coincides with the CSL data, supporting that the classical critical-state theory can be equivalently framed in terms of a critical fabric relation and a fabric-void ratio relation. It is worth to note that, in the original model [22], the fabric-void ratio relation is taken from O'hern et al. [12] which only depends on the coordination number drawn from isotropic or oedometric compression tests (shown as Eq.

(9)). The current study shows that this relation needs to be updated by the new FVS shown in Fig. 8 for general stress paths involving shear and compression.

In a more general context, many elastoplastic/hypoplastic models start to acknowledge soil fabric [7, 50-55] and are often formulated within the framework of anisotropic critical state theory (ACST) [7, 50-53]. In these models, the CSL in *e-p-q* space and the critical fabric are treated as separate conditions for attaining critical state, and thus the stress-dilatancy relation and fabric evolution laws are often proposed separately. The new FVS identified in this study, however, suggests that the evolution of fabric and void ratio (or dilatancy) are intrinsically coupled especially under monotonic loading. This finding should inspire more sensible and realistic stress-dilatancy-fabric relations in future elastoplastic models based on ACST.

It should be noted that the current FVS expressed in void ratio e and the first two invariants of second-order fabric tensor Z and F can only be used in modelling monotonic triaxial tests. The fabric-void ratio paths for cyclically loaded specimens do not collapse on the same FVS but are only attracted by it when monotonically sheared after the cyclic loading. We speculate that higher-order fabric tensors may contain some extra structural information for cyclically loaded specimens that are not captured by the second-order tensor studied in the current work. Establishing enriched descriptions of soil fabric based on contact, particle, and void vectors could be the first step in the follow-up studies along this line. In addition, further validation and investigation of FVS needs not only DEM simulations [16-18, 56, 57] but also advanced laboratory tests equipped with in-situ X-ray microtomography and other advanced imaging techniques [58-63].

7 Concluding remarks

The relationship between the contact fabric tensor E_{ij} and the void ratio of granular soils is studied by investigating the *e-Z-F* data of 137 DEM numerical tests. Among them, 8 consolidation and 80 true triaxial tests data is used for identifying a fabric-void ratio surface, and the rest 49 tests are used to verify the uniqueness of the FVS. A cyclic triaxial test is

458 employed to check whether the FVS observed from monotonic shearing is applicable when
459 stress reversal is included.

460 The results of the monotonic tests show that the usual *e-Z* relation of granular packings
461 is significantly influenced by the fabric anisotropy *F*. Such dependency can be conveniently
462 represented by a parametric surface, namely the fabric-void ratio surface, in the *e-Z-F* space.
463 The FVS consists of two separate parts with each describing the fabric-void ratio relation for
464 liquefied and non-liquefied soils. When static liquefaction happens, the fabric path suddenly
465 jumps from the non-liquefied portion of the FVS to the liquefied portion of the FVS. The
466 threshold coordination number (Z_{th}) that separates the liquefied and non-liquefied specimens
467 is found to be $Z_{th} = 2.73$. The proposed FVS is validated through an independent series of
468 consolidation and triaxial tests with different initial void ratios.

469 The fabric path of cyclically loaded specimen does not travel along the NL-FVS
470 established on the monotonic test results. This suggests that the two invariants of the 2nd rank
471 fabric tensor cannot completely tell the differences of soil structures induced by recent stress
472 reversals. After cyclic loading, sufficient monotonic loading can remove the effect of recent
473 stress history and thus recover the fabric-void ratio relation depicted by the FVS.

474 Revealing connections between the microstructural attributes and the macroscale
475 behaviours of granular is an ongoing endeavour for years. This study identifies an important
476 reference surface for correlating the void ratio with the fabric structure of frictional granular
477 materials and helps better understand the structural evolution of granular soils during
478 compaction and liquefaction. Future extensions of this work include: 1) incorporating higher
479 order fabric information to seek for a unique fabric-void ratio relation for both monotonically
480 and cyclically loaded specimens; 2) investigating the fabric state of liquefied soils and
481 understand its transition near the jamming point; 3) implement the concept of FVS in fabric-
482 centred constitutive theories of granular soils to unify the descriptions of critical state in
483 terms of void ratio and fabric tensors.

484

485

Acknowledgement

This research was supported by the U.S. National Science Foundation (NSF) under NSF CMMI Award No. 2113474.

Data Availability Statements

The datasets generated and analysed during the current study are available from the corresponding author on reasonable request.

References

1. Roscoe KH, Schofield AN, Wroth CP (1958) On The Yielding of Soils. Géotechnique 8(1):22-53.
2. Cubrinovski M, Ishihara K (2002) Maximum and minimum void ratio characteristics of sands. Soils and foundations 42(6):65-78.
3. Poulos SJ, Castro G, France JW (1985) Liquefaction evaluation procedure. Journal of Geotechnical Engineering 111(6):772-792.
4. Chang CS, Chao SJ, Chang Y (1995) Estimates of elastic moduli for granular material with anisotropic random packing structure. International journal of solids and structures 32(14):1989-2008.
5. Zhao J, Gao Z (2015) Unified anisotropic elastoplastic model for sand. Journal of Engineering Mechanics 142(1):04015056.
6. Gao Z, Zhao J (2017) A non-coaxial critical-state model for sand accounting for fabric anisotropy and fabric evolution. International Journal of Solids and Structures 106:200-212.
7. Li XS, Dafalias YF (2012) Anisotropic critical state theory: role of fabric. Journal of Engineering Mechanics 138(3):263-275.
8. Wang R, Fu P, Zhang J-M, Dafalias YF (2019) Fabric characteristics and processes influencing the liquefaction and re-liquefaction of sand. Soil Dynamics and Earthquake Engineering 125:105720.
9. Li X, Li XS (2009) Micro-Macro Quantification of the Internal Structure of Granular Materials. J Eng Mech 139(7):641-656.
10. Smith WO, Foote PD, Busang PF (1929) Packing of Homogeneous Spheres. Phys Rev 34(9):1271-1274.
11. Iwata H, Homma T (1974) Distribution of coordination numbers in random packing of homogeneous spheres. Powder Technol 10:79-83.
12. O'hern CS, Silbert LE, Liu AJ, Nagel SR (2003) Jamming at zero temperature and zero applied stress: The epitome of disorder. Phy Rev E 68(1):011306.
13. Suzuki M, Kada H, Hirota M (1999) Effect of size distribution on the relation between coordination number and void fraction of spheres in a randomly packed bed. Advan Powder Technol 10(4):353-365.
14. Yang RY, Zou RP, Yu AB (2000) Computer simulation of the packing of fine particles. Phy Rev E 62(3):3900-3908.
15. German RM (2014) Coordination number changes during powder densification. Powder Technol 253:368-376.
16. Gu X, Huang M, Qian J (2014) DEM investigation on the evolution of microstructure in granular soils under shearing. Granul Matter 16:91-106.
17. Nguyen HBK, Rahman MM, Fourie AB (2017) Undrained behaviour of granular material and the role of fabric in isotropic and K0 consolidations: DEM approach. Géotechnique 67(2):153-167.
18. Wang G, Wei J (2016) Microstructure evolution of granular soils in cyclic mobility

and post-liquefaction process. Granul Matter 18(3):1-13.
19. Rothenburg L, Kruyt NP (2004) Critical state and evolution of coordination number in simulated granular materials. Int J Solids Struct 41(21):5763-5774.
20. Kruyt NP (2012) Micromechanical study of fabric evolution in quasi-static deformation of granular materials. Mech Mater 44:120-129.
21. Huang X, Hanley KJ, O'sullivan C, Kwok CY, Wadee MA (2014) DEM analysis of the influence of the intermediate stress ratio on the critical-state behaviour of granular materials. Granul Matter 16(5):641-655.
22. Zhang Y, Zhou X, Wen Y (2020) Constitutive Theory for Sand Based on the Concept of Critical Fabric Surface. J Eng Mech 146(4):04020019.
23. Wen Y, Zhang Y (2021) Evidence of a Unique Critical Fabric Surface for Granular Soils. Géotechnique:published online. DOI: 10.1680/jgeot.1621.00126.
24. Šmilauer V, Catalano E, Chareyre B, Dorofeenko S, Duriez J, Dyck N, Eliáš J, Er B, Eulitz A, Gladky A, Guo N, Jakob C, Kneib F, Kozicki J, Marzougui D, Maurin R, Modenese C, Scholtès L, Sibille L, Stránský J, Sweijen T, Thoeni K, Yuan C (2021) Yade documentation 2nd ed.
25. Kuhn MR, Sun W, Wang Q (2015) Stress-induced anisotropy in granular materials: fabric, stiffness, and permeability. Acta Geotech 10(4):399-419.
26. Srivastava I, Silbert LE, Grest GS, Lechman JB (2020) Flow-Arrest Transitions in Frictional Granular Matter. Phy Rev Lett 122(4):048003.
27. Zhao S, Zhao J, Guo N (2020) Universality of internal structure characteristics in granular media under shear. Phy Rev E 101(1):012906.
28. Zhao J, Guo N (2013) Unique critical state characteristics in granular media considering fabric anisotropy. Géotechnique 63(8):695-704.
29. Thornton C, Antony SJ (2000) Quasi-static shear deformation of a soft particle system. Powder Technol 109(1):179-191.
30. Ng T (2006) Input Parameters of Discrete Element Methods. J Eng Mech 132(7):723-729.
31. Xie YH, Yang ZX, Barreto D, Jiang MD (2017) The influence of particle geometry and the intermediate stress ratio on the shear behavior of granular materials. Granul Matter 19(2):35.
32. Midi GDR (2004) On dense granular flows. Eur Phy J E 14(4):341-365.
33. Da Cruz F, Emam S, Prochnow M, Roux JN, Chevoir F (2005) Rheophysics of dense granular materials: discrete simulation of plane shear flows. Phy Rev E 72:021309.
34. Perez JCL, Kwok CY, O'sullivan C, Huang X, Hanley KJ (2016) Exploring the micro-mechanics of triaxial instability in granular materials. Géotechnique 66(9):725-740.
35. Guo N, Zhao J (2014) Local fluctuations and spatial correlations in granular flows under constant-volume quasistatic shear. Phy Rev E 89(4):042208.
36. Guo N, Zhao J (2013) The signature of shear-induced anisotropy in granular media. Comput Geotech 47:1-15.
37. Yang M, Taiebat M, Mutabaruka P, Radjaï F (2021) Evolution of granular materials under isochoric cyclic simple shearing. Phy Rev E 103(3):032904.

38. Kanatani K-I (1984) Distribution of directional data and fabric tensors. International Journal of Engineering Science 22(2):149-164.
39. Zhou W, Liu J, Ma G, Chang X (2017) Three-dimensional DEM investigation of critical state and dilatancy behaviors of granular materials. Acta Geotech 12(3):527-540.
40. Shi J, Guo P (2018) Fabric evolution of granular materials along imposed stress paths. Acta Geotech 13(6):1341-1354.
41. Kato S, Ishihara K, Towhata I (2001) Undrained shear characteristics of saturated sand under anisotropic consolidation. Soils Found 41(1):1-11.
42. Fourie AB, Tshabalala L (2005) Initiation of static liquefaction and the role of K0 consolidation. Can Geotech J 42(3):892-906.
43. Rabbi ATMZ, Rahman MM, Cameron DA (2018) Undrained Behavior of Silty Sand and the Role of Isotropic and K0 Consolidation. J Geotech Geoenviron Eng 144(4):04018014.
44. Wang R, Fu P, Zhang J-M, Dafalias YF (2016) DEM study of fabric features governing undrained post-liquefaction shear deformation of sand. Acta Geotech 11(6):1321-1337.
45. Arzt E (1982) The influence of an increasing particle coordination on the densification of spherical powders. Acta Metall 30(10):1883-1890.
46. Tory EM, Church BH, Tam MK, Ratner M (1973) Simulated random packing of equal spheres. Can J Chem Eng 51(4):484-493.
47. Zhang ZP, Liu LF, Yuan YD, Yu AB (2001) A simulation study of the effects of dynamic variables on the packing of spheres. Powder Technol 116(1):23-32.
48. Li XS, Wang Y (1998) Linear Representation of Steady-State Line for Sand. J Geotech Geoenviron Eng 124(12):1215-1217.
49. Nguyen HBK, Rahman MM, Fourie AB (2018) Characteristic Behavior of Drained and Undrained Triaxial Compression Tests: DEM Study. J Geotech Geoenviron Eng 144(9):04018060.
50. Yang Z, Liao D, Xu T (2020) A hypoplastic model for granular soils incorporating anisotropic critical state theory. International Journal for Numerical and Analytical Methods in Geomechanics 44(6):723-748.
51. Liao D, Yang Z (2021) Non-coaxial hypoplastic model for sand with evolving fabric anisotropy including non-proportional loading. International Journal for Numerical and Analytical Methods in Geomechanics 45(16):2433-2463.
52. Rahman MM, Dafalias YF (2021) Modelling undrained behaviour of sand with fines and fabric anisotropy. Acta Geotech.
53. Wang R, Cao W, Xue L, Zhang J-M (2021) An anisotropic plasticity model incorporating fabric evolution for monotonic and cyclic behavior of sand. Acta Geotech 16(1):43-65.
54. Hu N, Yu H-S, Yang D-S, Zhuang P-Z (2020) Constitutive modelling of granular materials using a contact normal-based fabric tensor. Acta Geotech 15(5):1125-1151.
55. Tafili M, Triantafyllidis T (2020) A simple hypoplastic model with loading surface

accounting for viscous and fabric effects of clays. International Journal for Numerical and Analytical Methods in Geomechanics 44(16):2189-2215.
56. Vairaktaris E, Theocharis AI, Dafalias YF (2020) Correlation of fabric tensors for granular materials using 2D DEM. Acta Geotech 15(3):681-694.
57. Wei J, Huang D, Wang G (2020) Fabric evolution of granular soils under multidirectional cyclic loading. Acta Geotech 15(9):2529-2543.
58. Druckrey AM, Imseeh WH, Alshibli KA (2021) Experimental evaluation of the anisotropic critical state theory for sand using 3D fabric evolution data of triaxial experiments. Acta Geotech.
59. Ganju E, Kılıç M, Prezzi M, Salgado R, Parab N, Chen W (2021) Effect of particle characteristics on the evolution of particle size, particle morphology, and fabric of sands loaded under uniaxial compression. Acta Geotech 16(11):3489-3516.
60. Imseeh WH, Druckrey AM, Alshibli KA (2018) 3D experimental quantification of fabric and fabric evolution of sheared granular materials using synchrotron micro-computed tomography. Granul Matter 20(2):24.
61. Wiebicke M, Andò E, Viggiani G, Herle I (2020) Measuring the evolution of contact fabric in shear bands with X-ray tomography. Acta Geotech 15(1):79-93.
62. Lenoir N, Bornert M, Desrues J, Bésuelle P, Viggiani G (2007) Volumetric Digital Image Correlation Applied to X-ray Microtomography Images from Triaxial Compression Tests on Argillaceous Rock. Strain 43(3):193-205.
63. Hall SA, Bornert M, Desrues J, Pannier Y, Lenoir N, Viggiani G, Bésuelle P (2010) Discrete and continuum analysis of localised deformation in sand using X-ray μCT and volumetric digital image correlation. Géotechnique 60(5):315-322.

List of symbols

a_1, a_2, a_3	parameters in the Gunary equation
A_1, A_2	parameter in the NL-FVS equation
b, b_e	principal stress ratio and principal strain ratio
$d, \bar{d}$	particle diameter and average particle diameter
e,	void ratio
e_0	initial void ratio taken at p = 50 kPa
e_c	critical-state void ratio
e_r	reference void ratio
e_{data}	void ratio of the DEM data
e_{FVS}	corresponding void ratios on the FVS of DEM data
E	particle Young's modulus
E_1, E_2, E_3	major, intermediate, and minor principal values of the second kind fabric tensor
E_{ij}	fabric tensor of the second kind
F	fabric anisotropy
F_c	critical-state fabric anisotropy
F_{data}	fabric anisotropy from DEM data
F_n, F_s	normal and tangential forces between two particles in contact
F_{ij}	fabric tensor of the third kind
G_{ij},	fabric tensor of the first kind
h	parameter in the O'Hern equation
h_r	parameter in the NL-FVS equation
I	inertia number
k_n, k_s	normal and tangential stiffness of a particle
K_n, K_s	normal and tangential stiffness of a contact
M_c, M_e	critical stress ratio at compression and extension
n, n_r	porosity and reference porosity
$\mathbf{n}$	unit contact normal vector
N	number of loading cycles in cyclic triaxial test
N_c,	number of contacts
N_p	number of particles in the assembly
p	mean effective stress
p_a	atmosphere pressure
p_c	mean effective stress at the end of consolidation or the beginning of triaxial shearing
q	deviatoric stress
R	particle radius
Z,	coordination number
Z_c	critical-state coordination number
Z_r	coordination number at reference porosity
Z_{data}	coordination number from DEM data
Z_{th},	threshold coordination number that distinguish the liquefied and non-liquefied state
δ_n, δ_s	normal and tangential displacement of a contact
δ_{ij}	Kronecker delta
Δt_{cr}	critical time step

ε_1, ε_2, ε_3	major, intermediate, and minor principal strain
ε_a	axial strain
$\dot{\varepsilon}$	strain rate
η, η_0	deviatoric stress ratio and the deviatoric stress ratio during consolidation
θ_E	fabric lode angle
λ	parameter in the equation of *e-p* normal consolidation line
μ	particle friction coefficient after the initial compaction with p > 5kPa
μ_0	particle friction coefficient during the initial compaction with p <= 5kPa
ξ	parameter in the equation of *e-p* normal consolidation line
ρ	directional distribution of contact normals
$\bar{\rho}_c$	directional distribution density of contact normals
ρ_g	particle density
σ_1, σ_2, σ_3	major, intermediate, and minor principal stress
φ	parameter in the O'Hern equation
ζ	parameter in the NL-FVS equation
Γ	maximum void ratio in the equation of *e-p* normal consolidation line
Ω	solid angle

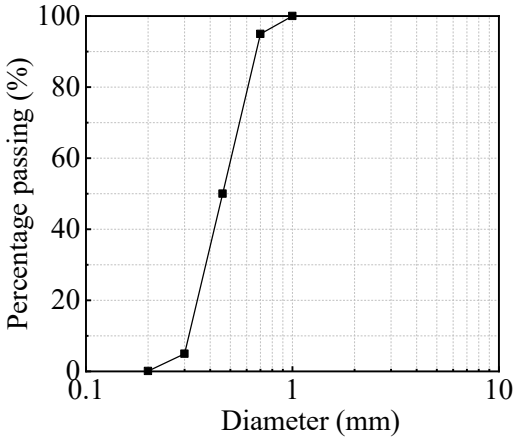

Fig. 1. Grain size distribution of the DEM specimen used in this study.

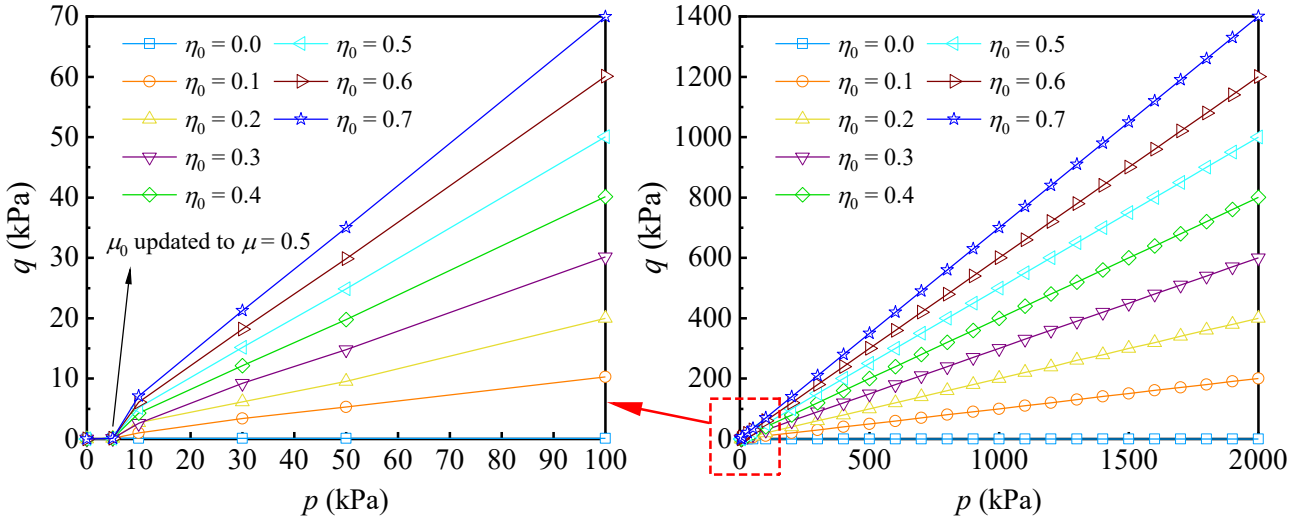

Fig. 2. Stress paths of consolidation tests.

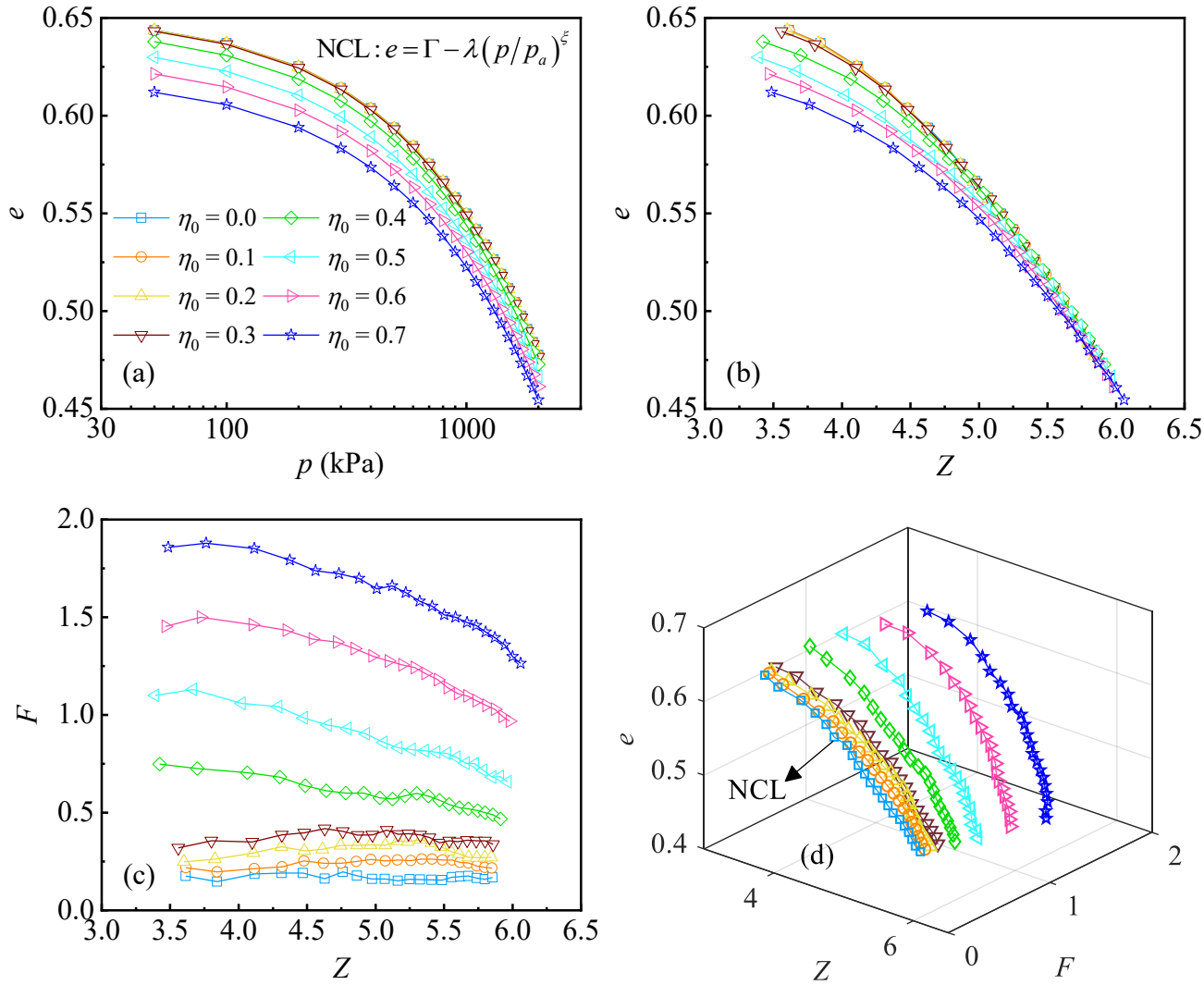

Fig. 3. (a) Consolidation lines in *e-p* plane, (b) consolidation lines in *e-Z* plane, (c) fabric paths in *Z-F* plane, (d) fabric-void ratio paths in *e-Z-F* space.

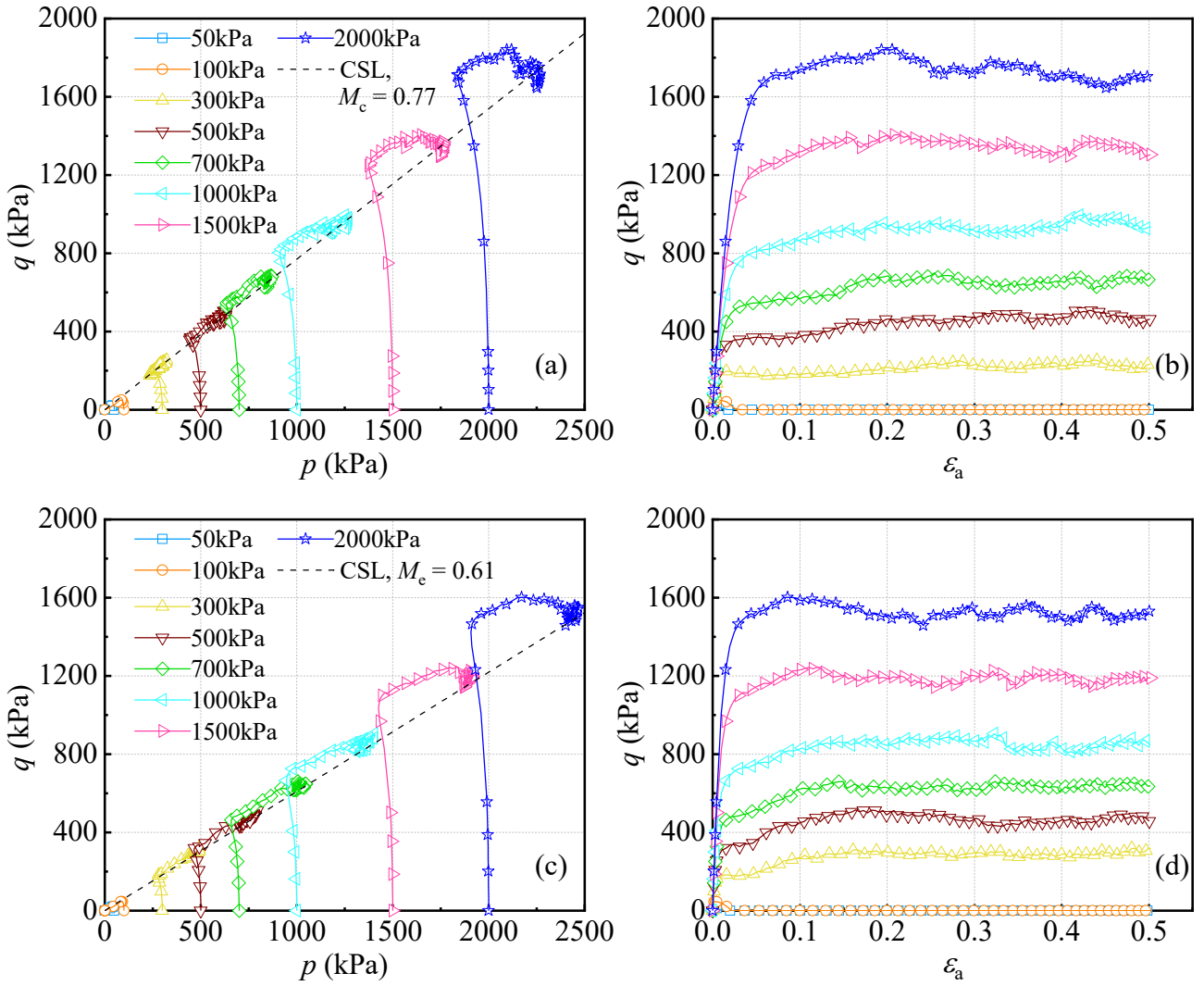

Fig. 4. Stress and strain evolution of CIU tests: (a) stress of b_e = 0 tests, (b) stress-strain of b_e = 0 tests, (c) stress of b_e = 1 tests, (d) stress-strain of b_e = 1 tests.

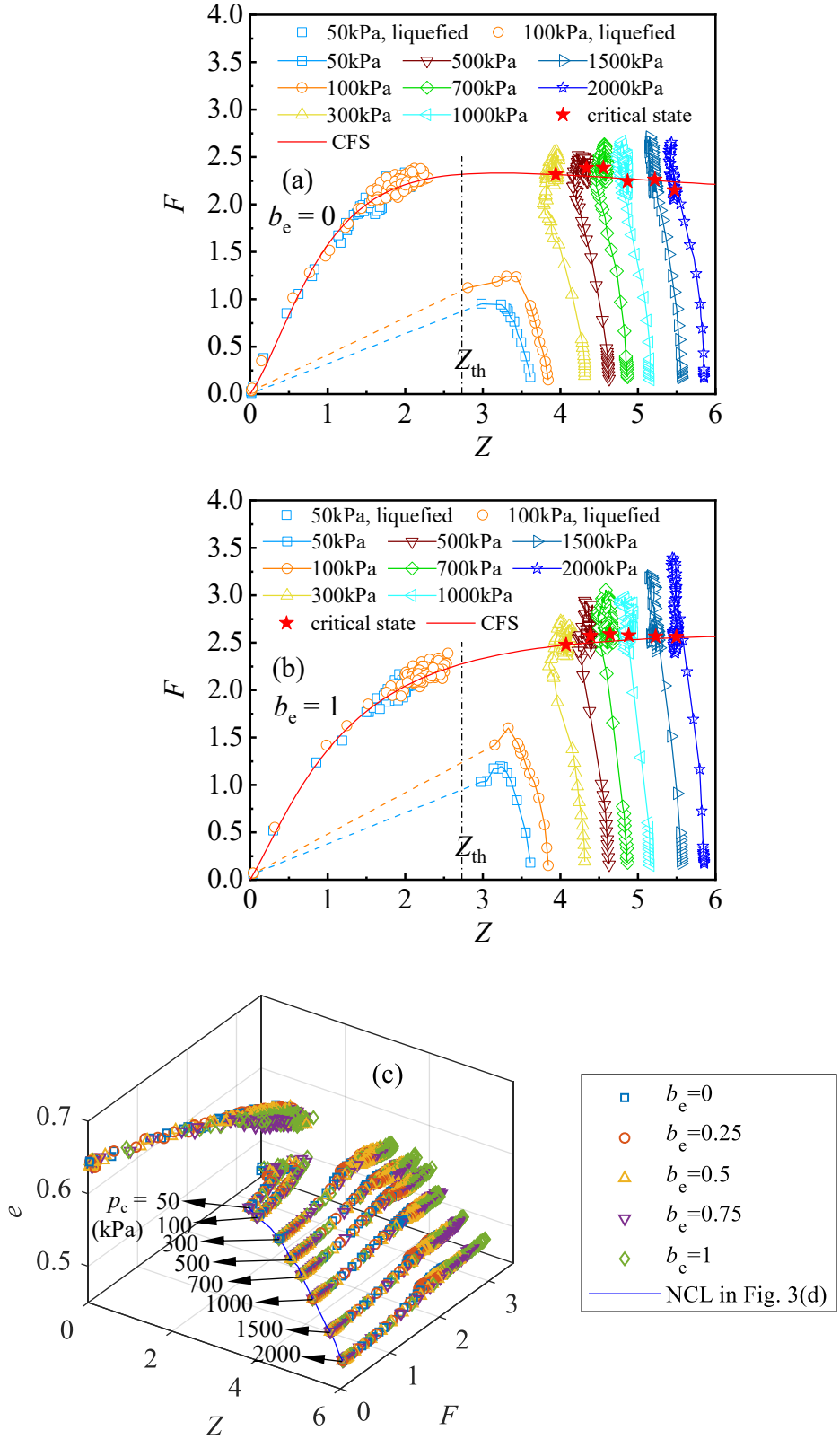

Fig. 5. Fabric evolution of CIU tests: (a) *Z*-*F* relation of $b_e = 0$ tests, (b) *Z*-*F* relation of $b_e = 1$ tests, (c) fabric-void ratio paths of $b_e = 0 \sim 1$ tests.

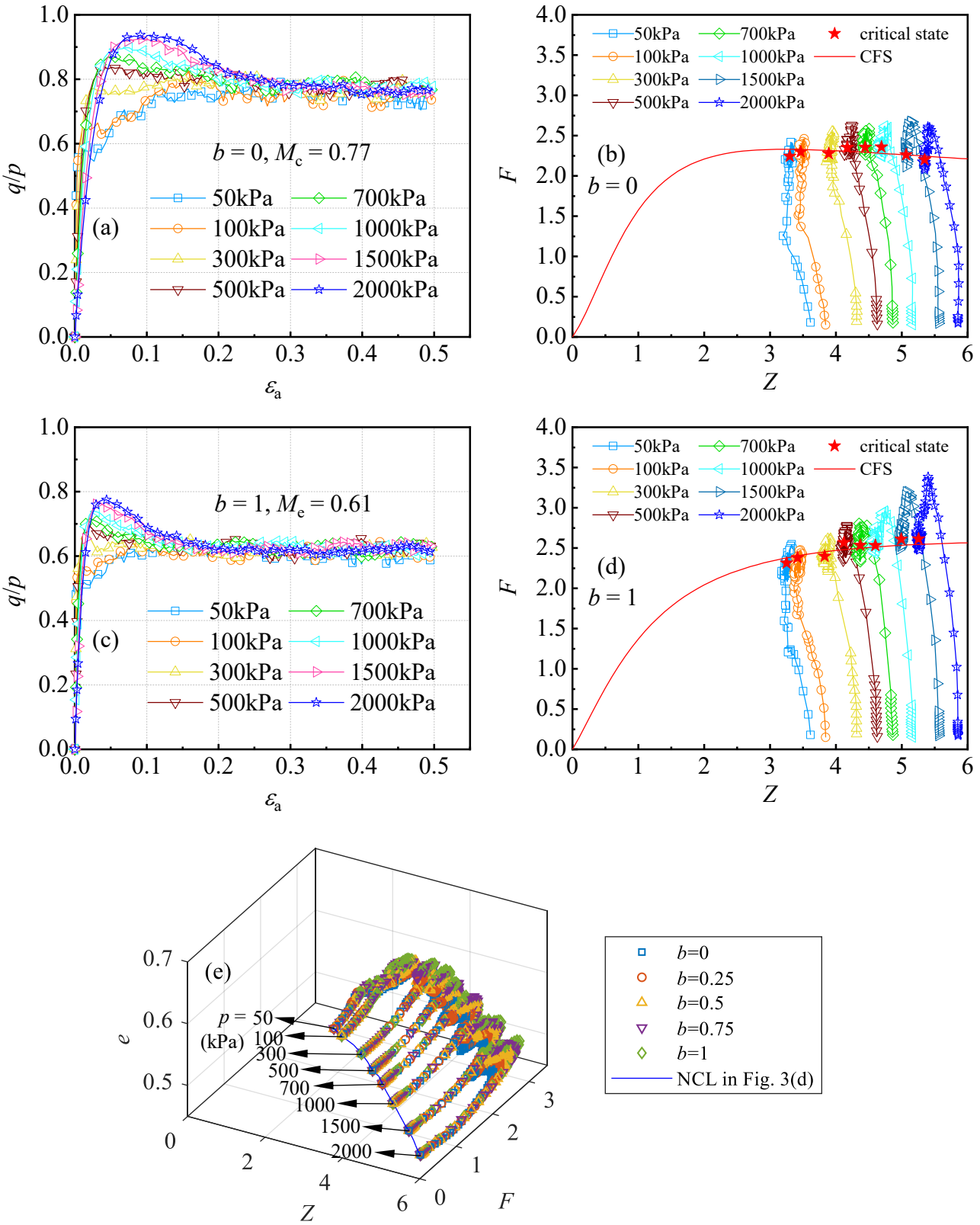

Fig. 6. Evolution of CID tests: (a) stress-strain of b = 0 tests, (b) fabric paths of b = 0 tests, (c) stress-strain of b =1 tests, (d) fabric paths of b = 1 tests, (e) fabric-void ratio paths of b = 0 ~ 1 tests.

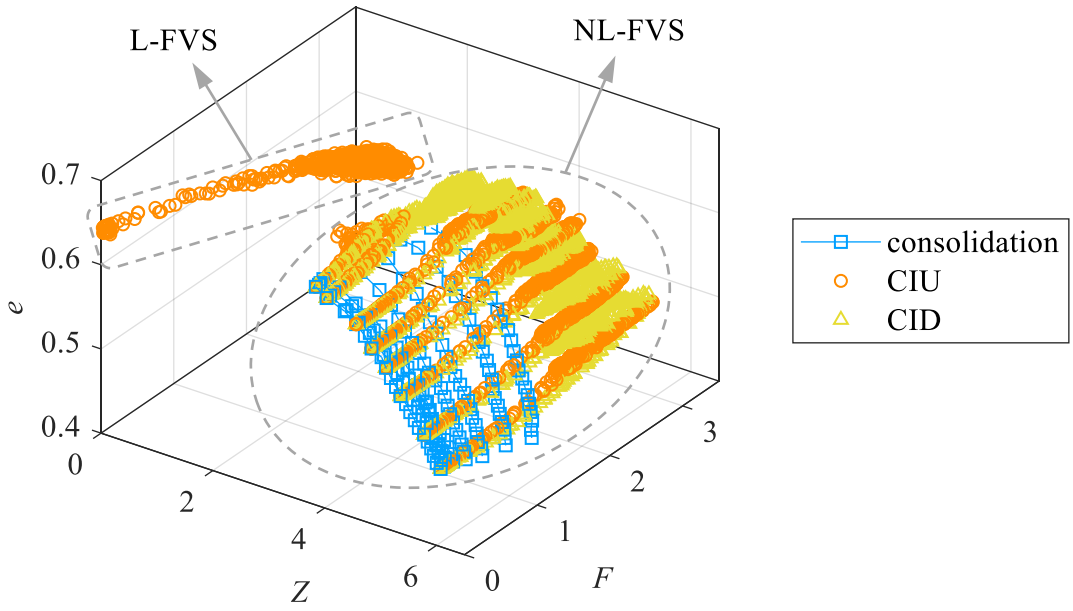

Fig. 7. Compiled fabric-void ratio data from consolidation, CIU, and CID tests.

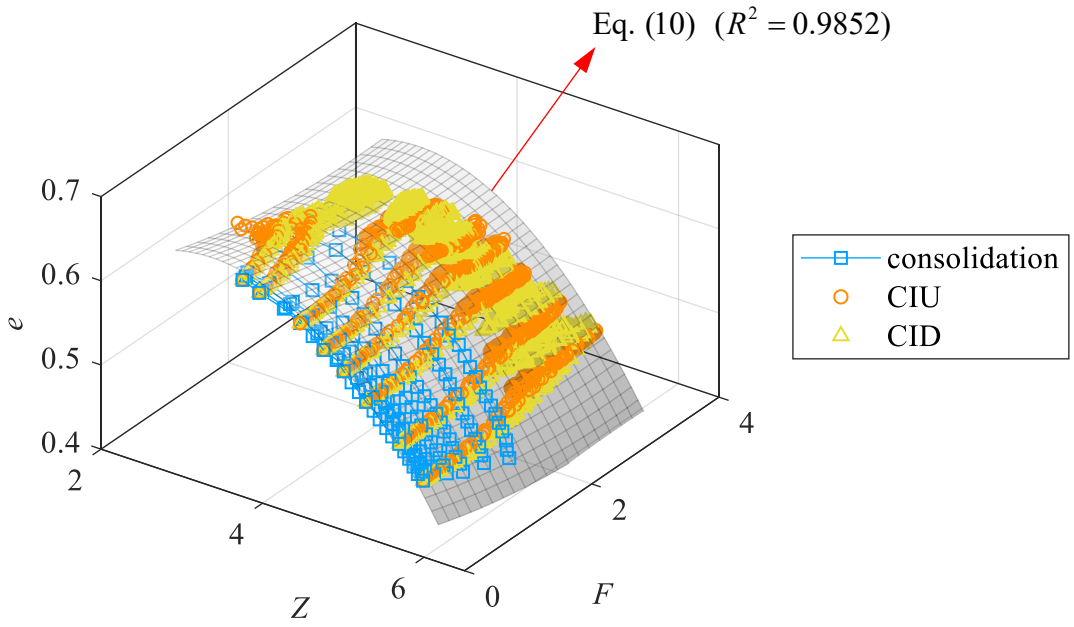

Fig. 8. Mathematical description of the non-liquefied fabric-void ratio surface.

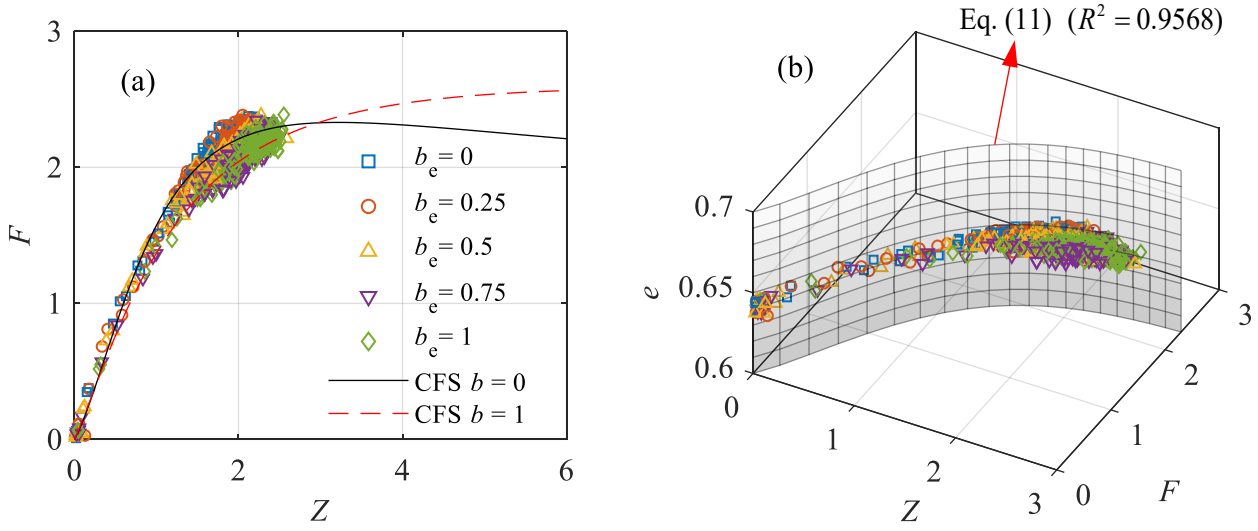

Fig. 9. Mathematical description of the liquefied fabric-void ratio surface in (a) *Z-F* plane and (b) *e-Z-F* space.

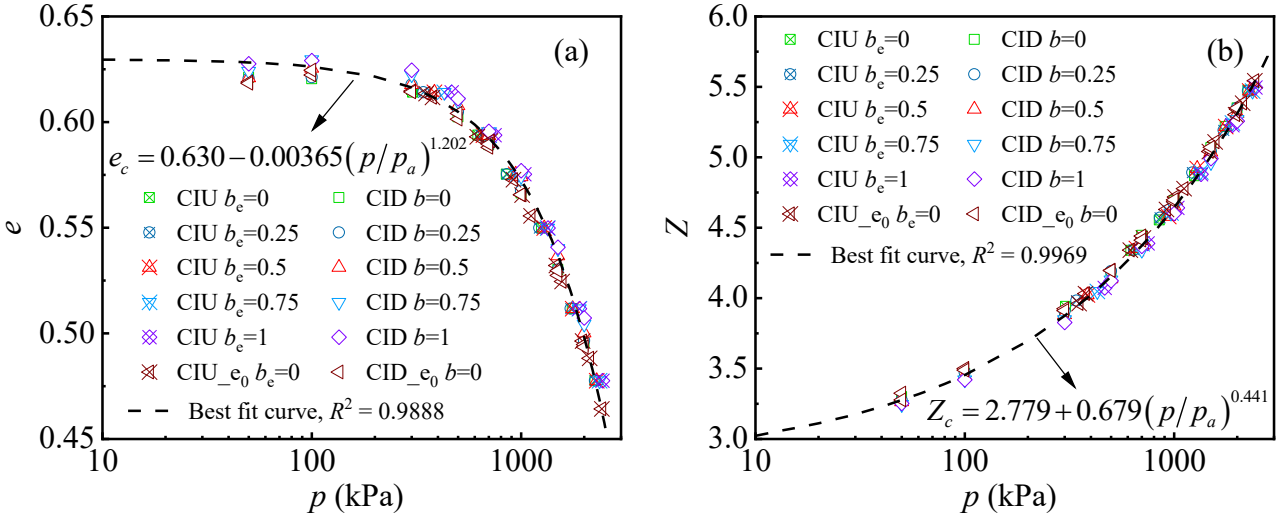

Fig. 10. Critical state lines of CIU, CID, CIU_e_0, and CID_e_0 tests in (a) *e-p* plane and (b) *Z-p* plane.

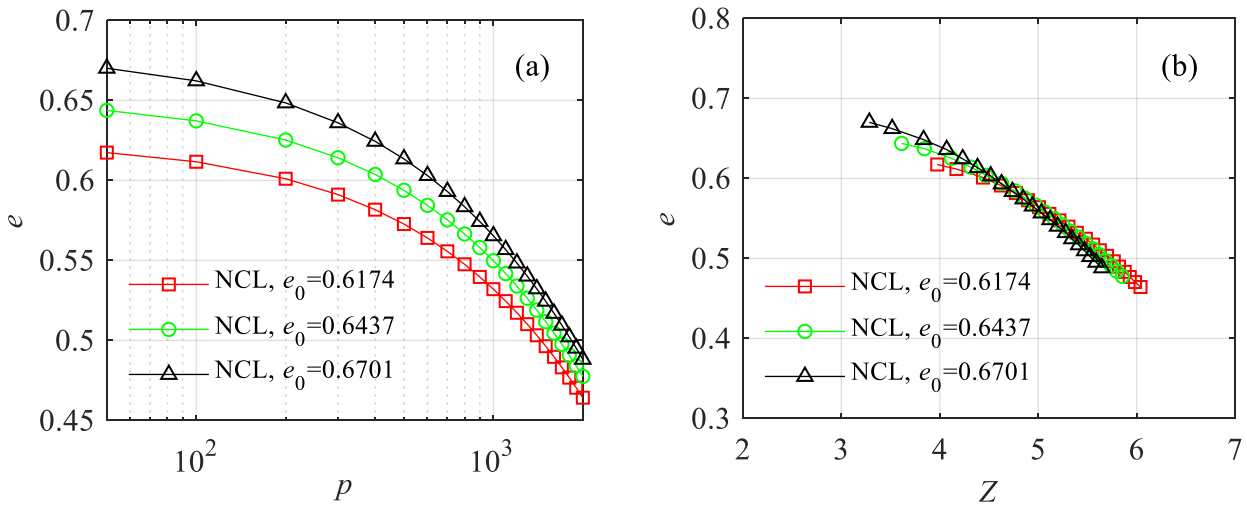

Fig. 11. NCLs of specimens with different initial density in (a) *e-p* plane and (b) *e-Z* plane.

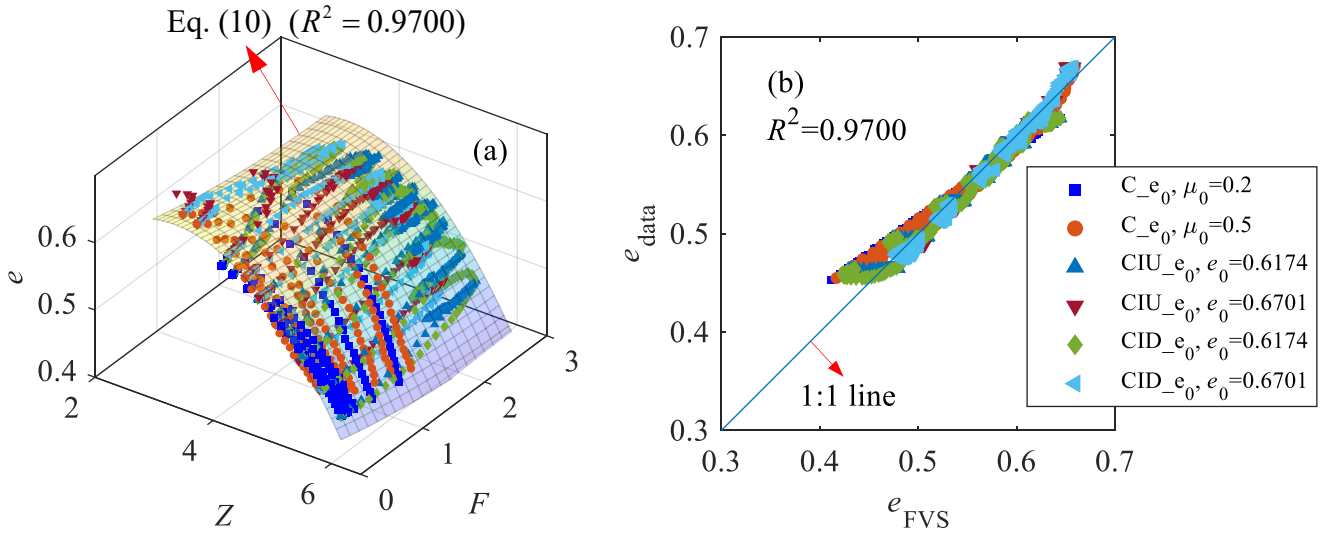

Fig. 12. Validation of NL-FVS by C_e_0, CIU_e_0 and CID_e_0 tests: (a) FVS and fabric-void ratio data, (b) comparison between the void ratio data and those calculated by the FVS equation.

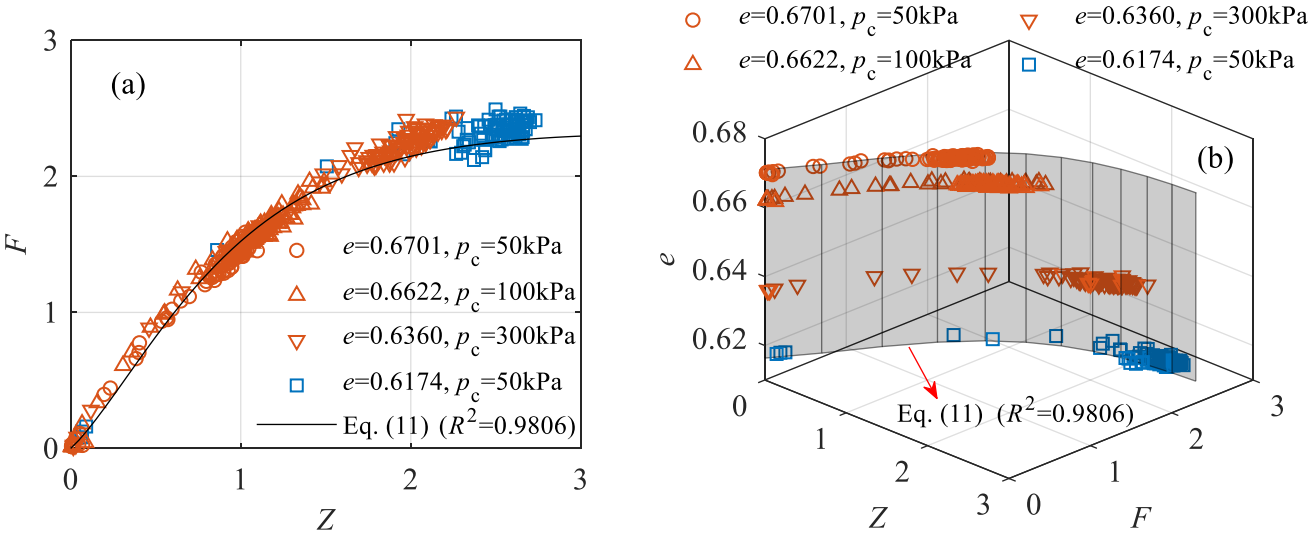

Fig. 13. Validation of L-FVS by CIU_e_0 test data in (a) *Z-F* plane and (b) *e-Z-F* space.

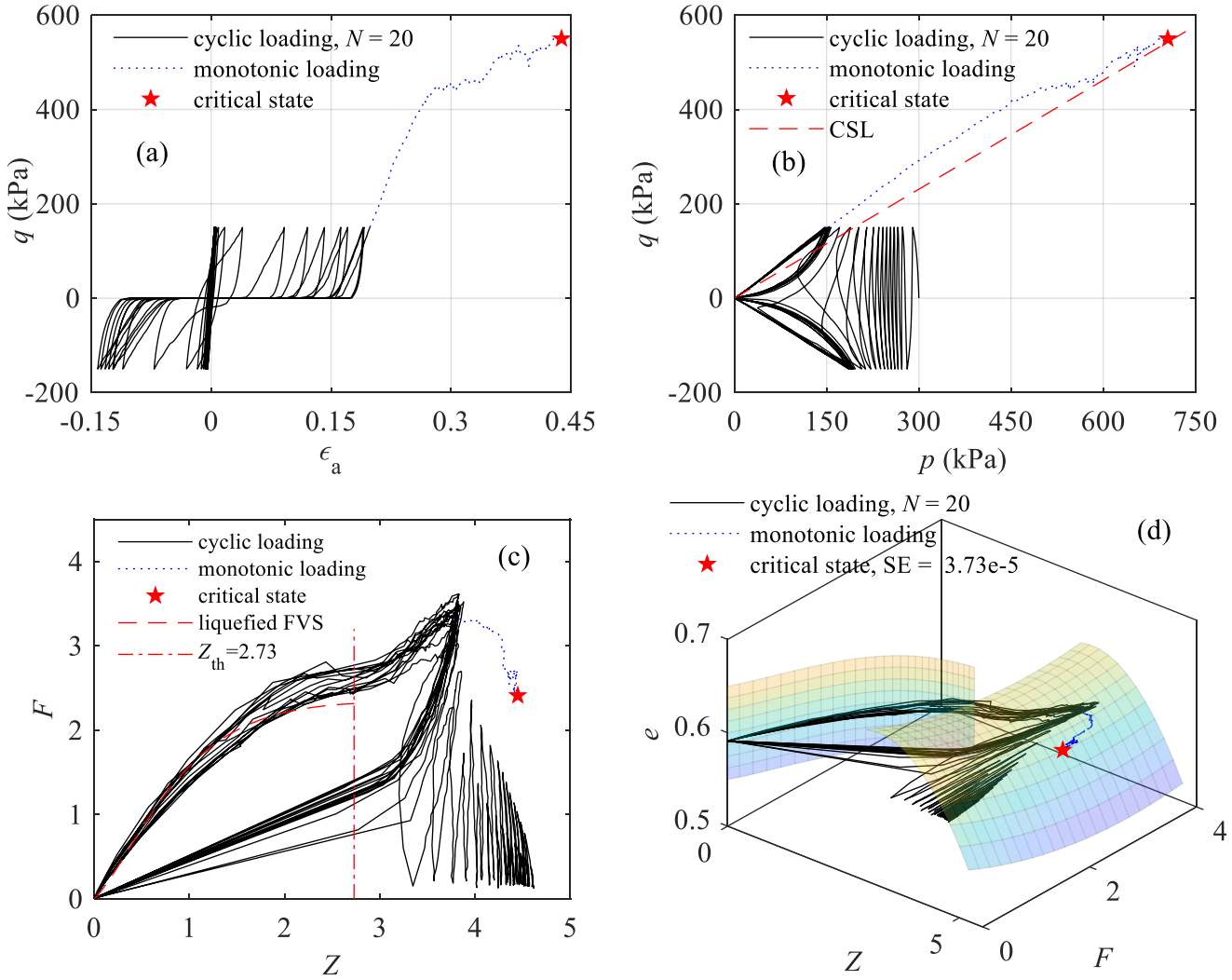

Fig. 14. Evolution of CIUC test in: (a) stress-strain plane, (b) stress plane, (c) fabric plane, (d) fabric-void ratio space.

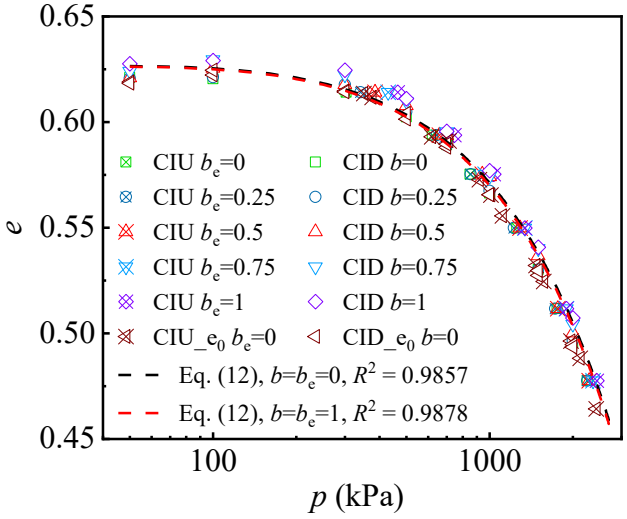

Fig. 15. Comparison between the derived CSL in *e-p* plane the DEM critical-state data in Fig. 10(a)

Table 1. Summary of consolidation, CIU and CID tests

Test series	consolidation	CIU	CID
p_c (kPa)	50 ~ 2000	50, 100, 300, 500, 700, 1000, 1500, 2000	50, 100, 300, 500, 700, 1000, 1500, 2000
μ_0	0.3	0.3	0.3
η_0	0, 0.1, 0.2, 0.3, 0.4, 0.5, 0.6, 0.7	0	0
b or b_e	N/A	b_e = 0, 0.25, 0.5, 0.75, 1	b = 0, 0.25, 0.5, 0.75, 1
Tests number	8	40	40

Table 2. Summary of C_e_0, CIU_e_0 and CID_e_0 tests

Test series	C_e_0	CIU_e_0	CID_e_0
p_c (kPa)	50 ~ 2000	50, 100, 300, 500, 700, 1000, 1500, 2000	50, 100, 300, 500, 700, 1000, 1500, 2000
μ_0	0.2, 0.5	0.2, 0.5	0.2, 0.5
η_0	0, 0.1, 0.2, 0.3, 0.4, 0.5, 0.6, 0.7	0	0
b or b_e	N/A	0	0
Tests number	16	16	16